Spin-valley blockade in carbon nanotube double quantum dots

András Pályi[1,2] and Guido Burkard[1]
[1]*Department of Physics, University of Konstanz, D-78457 Konstanz, Germany*
[2]*Department of Materials Physics, Eötvös University–Budapest, P.O. Box 32, H-1517 Budapest, Hungary*
(Received 15 May 2010; published 14 October 2010)

We present a theoretical study of the Pauli or spin-valley blockade for double quantum dots in semiconducting carbon nanotubes. In our model, we take into account the following characteristic features of carbon nanotubes: (i) fourfold (spin and valley) degeneracy of the quantum-dot levels, (ii) the intrinsic spin-orbit interaction which is enhanced by the tube curvature, and (iii) valley mixing due to short-range disorder, i.e., substitutional atoms, adatoms, etc. We find that the spin-valley blockade can be lifted in the presence of short-range disorder, which induces two independent random (in magnitude and direction) valley-Zeeman fields in the two dots, and hence acts similarly to hyperfine interaction in conventional semiconductor quantum dots. In the case of strong spin-orbit interaction, we identify a parameter regime where the current as the function of an applied axial magnetic field shows a zero-field dip with a width controlled by the interdot tunneling amplitude, in agreement with recent experiments.

DOI: 10.1103/PhysRevB.82.155424 PACS number(s): 73.63.Kv, 73.63.Fg, 73.23.Hk, 71.70.Ej

I. INTRODUCTION

Recent developments of experimental techniques allow for preparation, manipulation, and readout of few-electron spin states in quantum dots (QDs),[1] indicating the strong potential of these systems for future application in quantum information processing.[2] A major factor limiting the performance of quantum-dot spin qubits in widely used III-V semiconductors (e.g., GaAs) is spin decoherence due to hyperfine interaction with nuclear spins. A strategy to suppress spin decoherence is to use QDs dominantly consisting of nuclear-spin-free isotopes of group IV materials. Carbon structures, such as carbon nanotubes (CNTs) or graphene, are prime candidates for that purpose as the natural abundance of spin-carrying ^{13}C nuclei is very small (1%). This observation has motivated intensive theoretical investigation[3–14] and the experimental realization of QDs in carbon nanostructures.[14–29] Further perspectives of carbon-based quantum information processing have been opened by proposals suggesting to utilize the valley degree of freedom of the delocalized electrons as a qubit,[30,31] and to exploit the interplay of spin-orbit interaction, valley mixing, and the bending of CNTs for implementing qubit operations.[32]

The Pauli blockade or spin blockade effect[1,33] in conventional semiconductor double QDs (DQDs) has provided a distinct probe of spin physics in these devices and has been utilized in the past decade for various purposes in the context of spin qubits. A basic application is spin-state initialization and readout in experiments realizing resonant manipulation of single spins.[34–36] Pulsed-gate techniques combined with the spin blockade setup have been used[37–39] in qubit manipulation experiments where the information was encoded in the two-electron spin states S and T_0 or S and T_+. Similar experiments have been utilized to prepare the state of the nuclear-spin ensemble of the crystal lattice, with the aim of prolonging the decoherence time of the qubit.[40–42] Furthermore, spin blockade has been proven an efficient tool to gain information about the mechanisms of spin relaxation and decoherence, and the corresponding energy scales. In particular, it has been applied to measure the energy scales of hyperfine[43,44] and spin-orbit interactions.[45,46] The implementation of this range of functionalities in carbon-based quantum dots, potentially showing improved qubit performance, is an intense ongoing effort.[20–22,29]

In this work, we consider Pauli blockade in a transport setup,[1,33] where electrons are transmitted from the source to the drain in a serially coupled DQD via the $(0,1)\rightarrow(1,1)\rightarrow(0,2)\rightarrow(0,1)$ cycle (Fig. 1). Here (n_L,n_R) denotes the charge state with n_L (n_R) electrons in the left (right) QD. In conventional semiconductor DQDs, if the (1,1) and (0,2) states are aligned in energy, then states sharing the same spin state become hybridized due to interdot tunneling. The only energetically available (0,2) state has a singlet spin state, therefore it hybridizes with the (1,1) singlet only, leaving the three (1,1) triplet states without a (0,2) component. This implies that whenever a (1,1) triplet state is occupied in the transport process the current is blocked since the (1,1) triplet state cannot decay to a (0,1) state: the occupation of (1,0) states is energetically forbidden and the source connected to dot L cannot absorb the electron. The blockade can be lifted by various mechanisms influencing spin dynamics, e.g., hyperfine interaction, spin relaxation, etc., resulting in a non-

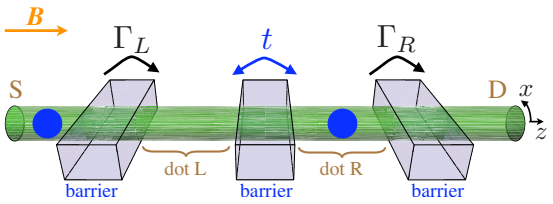

FIG. 1. (Color online) Schematic of the spin-valley blockade setup with a carbon nanotube double quantum dot and an external magnetic field $\boldsymbol{B}$ aligned with the tube axis. In this regime electrons are transported from source (S) to drain (D) while the DQD occupancy changes between single and double. Spots represent electrons; the figure shows the (0,1) charge configuration of the double dot. Lead-dot tunneling rates Γ_L, Γ_R and interdot tunneling amplitude t are indicated.

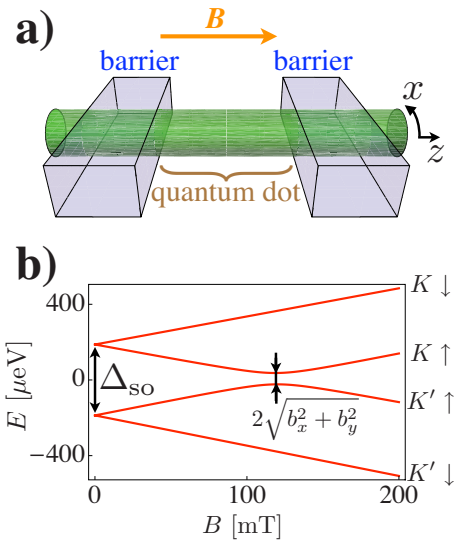

FIG. 2. (Color online) (a) Schematic of a quantum dot in a carbon nanotube, with an external magnetic field $\boldsymbol{B}$ aligned with the tube axis. (b) Magnetic-field dependence of the spin-orbit-split single-electron ground state sublevels of a nanotube quantum dot, obtained from diagonalizing $H_0+H_{\mathrm{eff,dis}}$ [see Eqs. (5) and (9)]. Spin and valley quantum numbers of the energy levels are indicated on the right.

zero steady-state current, termed as the "leakage current,"[1] through the DQD.

This explanation is altered in the case of electrostatically defined CNT DQDs (Fig. 1) where the valley degeneracy of the electronic spectrum is maintained,[10,21] resulting in fourfold-degenerate (spin and valley) quantum-dot energy levels (see Fig. 2). In this case the six (0,2) states have *combined spin-valley wave functions* which are antisymmetric under particle exchange. We refer to such states as *supersinglets*. The 16-dimensional (1,1) subspace can be separated to a six-dimensional supersinglet subspace and a ten-dimensional subspace of combined spin-valley wave functions being symmetric under particle exchange, i.e., *supertriplets*. Hybridization occurs between the (0,2) states and the (1,1) supersinglets, and the (1,1) supertriplets do not acquire any (0,2) components. As discussed above for the case of conventional semiconductor DQDs, this leads to a blockade of the transport. The blockade can be lifted by various mechanisms affecting the spin and valley dynamics. To distinguish the cases of conventional and CNT DQDs, we refer to them as spin blockade and spin-valley blockade in the following, respectively.

Here we focus on recent experiments[21,22] observing the spin-valley blockade in clean CNT DQDs with natural (1%) and enriched (99%) ^{13}C abundance. Charge sensing data[21] indicates that in these samples the valley degeneracy was maintained in contrast to other observations.[20,29] In the case of the isotope-enriched samples, a zero-field peak has been observed[22] in the magnetic-field dependence of the leakage current at small interdot tunneling. Following a model developed for GaAs DQDs,[44] this feature has been attributed to hyperfine interaction, although the corresponding energy scale inferred from the measurement is two orders of magnitude larger than the theoretical estimates.[6,47] This discrepancy has not yet been explained. At large interdot tunneling, the observed magnetotransport data show a zero-field dip[21,22] with a width controlled by the transparency of the interdot tunneling barrier, irrespective of the dominant isotope species. In InAs DQDs, a similar feature has been measured recently,[45,48] and good agreement has been found with a phenomenological model incorporating spin-orbit-enabled spin-flip interdot tunneling and spin relaxation.[46] The same mechanism might be responsible for the observed magnetotransport in CNT DQDs as well.

In this work, we provide an alternative explanation of the zero-field dip found in the magnetotransport curve of CNT DQDs in the spin-valley blockade regime. Using a microscopic model, we argue that the disorder-induced valley dynamics is different in the two dots, resulting in the lifting of the spin-valley blockade and allowing for a finite current through the DQD. In this mechanism, disorder plays a role analogous to hyperfine interaction in conventional semiconductor DQDs.

To show this, we set up a model Hamiltonian for the DQD accounting for the following unconventional properties of CNT QDs: (i) fourfold (spin and valley) degeneracy of the QD energy levels, (ii) the intrinsic spin-orbit interaction which is enhanced by the tube curvature and induces an energy splitting between Kramers pairs, and (iii) valley mixing due to short-range disorder, i.e., substitutional atoms, adatoms, etc. We provide a microscopic analysis of property (iii), resulting in an effective Hamiltonian for a single fourfold degenerate QD level. We find that disorder appears in this Hamiltonian as a random (in magnitude and direction) effective magnetic field acting on the valley degree of freedom. We express this valley-Zeeman field as a function of the disorder configuration and the envelope function of the electron occupying the QD. Our transport calculations are based on a Born-Markov master equation. The main finding of this work is that the disorder-induced valley-Zeeman fields provide a mechanism that lifts the spin-valley blockade. Depending on the relative significance of spin-orbit interaction and disorder, we identify different patterns in the magnetic-field dependence of the steady-state current. In the case of strong spin-orbit interaction, we find a zero-field dip in the magnetotransport curve, in agreement with recent experiments, however our model does not include spin-flip tunneling or spin-relaxation processes. In the case of strong disorder, we find that the magnetotransport curve can show both a zero-field dip and peak, depending on the disorder configuration.

The rest of the paper is organized as follows. In Sec. II, we provide a microscopic analysis of short-range disorder in a CNT QD. In Sec. III, the model Hamiltonian of the CNT DQD and the master-equation approach is described. In Secs. IV and V, we study the magnetotransport in the spin-valley blockade regime in the cases of strong spin-orbit interaction and strong disorder, respectively. Our conclusions are presented in Sec. VI.

II. SHORT-RANGE DISORDER IN THE QUANTUM-DOT HAMILTONIAN

In this section, we consider a single electrostatically defined QD in a semiconducting CNT, in the presence of a

homogeneous magnetic field. Our aim is to derive a 4×4 effective Hamiltonian describing the effect of the short-range disorder present in the CNT on a fourfold (spin and valley) degenerate state of the QD. We show that in this effective Hamiltonian the short-range disorder appears as an effective magnetic (Zeeman) field acting on the valley degree of freedom, and having a random magnitude and direction.

First we consider a CNT QD model without spin-orbit interaction and short-range disorder. We choose the z axis of the coordinate system as aligned with the axis of the CNT, and the x coordinate is measured along the circumference of the nanotube as indicated in Fig. 2(a).

The four tight-binding wave functions, corresponding to a fourfold-degenerate single-particle energy level of the QD have the form[49]

$$(\psi_{vs})_{l\sigma} \equiv (\psi_v)_{l\sigma}\chi_s = \sqrt{\Omega_{\text{cell}}}e^{i(v\boldsymbol{K}\cdot\boldsymbol{r}_{l\sigma}+\varphi_{v\sigma})}\Psi_\sigma^{(v)}(\boldsymbol{r}_{l\sigma})\chi_s, \quad (1)$$

where $s\in(\uparrow,\downarrow)\equiv(+,-)$ and $v\in(K,K')\equiv(+,-)$ are spin and valley quantum numbers. Furthermore, $\sigma\in\{A,B\}$ is the sublattice index, l is the unit-cell index, Ω_{cell} is the unit-cell area, $\boldsymbol{r}_{l\sigma}=(x_{l\sigma},z_{l\sigma})$ is the position of the carbon atom on sublattice σ in the lth unit cell, the phase factors[49] in the exponential are $\varphi_{K,A}=\varphi_{K',B}=0$, $\varphi_{K',A}=\eta$, and $\varphi_{K,B}=\eta-\pi/3$ with η being the chiral angle of the CNT, and $\chi_+=(1,0)$ and $\chi_-=(0,1)$ are the two possible spin states with axial polarization. The four smoothly varying envelope functions $\Psi_\sigma^{(v)}$ can be obtained by solving the Dirac-type envelope function equations[49] for $v\in(+,-)$,

$$[v_F(\sigma_x p_x + v\sigma_y p_z) + V_{\text{conf}}(z)]\begin{pmatrix}\Psi_A^{(v)}\\ \Psi_B^{(v)}\end{pmatrix} = E\begin{pmatrix}\Psi_A^{(v)}\\ \Psi_B^{(v)}\end{pmatrix}. \quad (2)$$

Here σ_x and σ_y are Pauli matrices, corresponding to the sublattice degree of freedom and $V_{\text{conf}}(z)$ is a smooth confinement potential, e.g., induced by electrostatic gates. Note that our choice of the coordinate system [see Fig. 2(a)] implies that p_z (and not p_y) appears in the envelope Hamiltonian. The functions $\Psi_\sigma^{(v)}$ and ψ_{vs} are normalized,

$$1 = \int_0^{2\pi R} dx \int_{-\infty}^{\infty} dz(|\Psi_A^{(v)}(\boldsymbol{r})|^2 + |\Psi_B^{(v)}(\boldsymbol{r})|^2), \quad (3a)$$

$$1 = \sum_{l\sigma} (\psi_{vs})_{l\sigma}^\dagger(\psi_{vs})_{l\sigma}, \quad (3b)$$

where R is the radius of the nanotube.

Our goal is to set up a 4×4 effective Hamiltonian describing the valley mixing due to short-range disorder. Short-range disorder can be caused by any kind of atomic faults of the crystalline structure: substitutional or interstitial atoms, vacancies, adatoms, etc. We take into account short-range disorder in the tight-binding model as a static random on-site potential V_i, i.e., $(H_{\text{dis,TB}})_{i,j}=V_i\delta_{ij}$. [$i=(l\sigma)$ is an index combining the unit cell index l and the sublattice index σ.] Without the loss of generality, we can assume that the disorder potential has zero mean, $\langle V_i\rangle=0$. The short-range impurities are typically charge neutral, and therefore the interaction between them is weak. This suggests that the random on-site potential is spatially uncorrelated, $\langle V_iV_j\rangle=\delta_{ij}\langle V_i^2\rangle$. A further plausible assumption is that the CNT is homogeneous. Motivated by these observations, we model the disorder potential on the different sites as independent and identically distributed random variables. Since we focus on valley effects, we neglect possible sources of spin-dependent short-range disorder, such as hyperfine interaction due to ^{13}C atoms[10] and adatom-enhanced spin-orbit interaction,[50] for example.

To derive an effective 4×4 Hamiltonian describing the effect of the short-range disorder, we project the tight-binding disorder Hamiltonian $H_{\text{dis,TB}}$ onto the four-dimensional subspace of interest. The corresponding projector is

$$P = \sum_{vs} |\psi_{vs}\rangle\langle\psi_{vs}|. \quad (4)$$

The same method has been used recently by us to analyze the effect of hyperfine interaction in carbon-based QDs.[10] The obtained effective Hamiltonian is

$$H_{\text{dis,eff}} = PH_{\text{dis,TB}}P = (b_0\tilde{\tau}_0 + b_x\tilde{\tau}_x + b_y\tilde{\tau}_y + b_z\tilde{\tau}_z)\otimes s_0 \equiv (b_0\tilde{\tau}_0 + \boldsymbol{b}\cdot\tilde{\boldsymbol{\tau}})\otimes s_0, \quad (5)$$

where

$$b_k = \Omega_{\text{cell}}\sum_{l\sigma} V_{l\sigma}F_{l\sigma}^{(k)} \quad (6)$$

for $k\in\{0,x,y,z\}$. Here, $F_{l\sigma}^{(0)}=\Sigma_v|\Psi_\sigma^{(v)}(\boldsymbol{r}_{l\sigma})|^2/2$, $F_{l\sigma}^{(z)}=\Sigma_v v|\Psi_\sigma^{(v)}(\boldsymbol{r}_{l\sigma})|^2/2$, and $F_{l\sigma}^{(x/y)}=\text{Re/Im}\times[e^{2i\boldsymbol{K}\cdot\boldsymbol{r}_{l\sigma}}e^{i(\varphi_{+\sigma}-\varphi_{-\sigma})}\Psi_\sigma^{(-)*}(\boldsymbol{r}_{l\sigma})\Psi_\sigma^{(+)}(\boldsymbol{r}_{l\sigma})]$. The operators $\tilde{\tau}_{0,x,y,z}$ are natural representations of the Pauli matrices on the two-dimensional Hilbert space spanned by ψ_K and $\psi_{K'}$, i.e.,

$$\tilde{\tau}_0 = |\psi_K\rangle\langle\psi_K| + |\psi_{K'}\rangle\langle\psi_{K'}|, \quad (7a)$$

$$\tilde{\tau}_x = |\psi_K\rangle\langle\psi_{K'}| + |\psi_{K'}\rangle\langle\psi_K|, \quad (7b)$$

$$\tilde{\tau}_y = -i|\psi_K\rangle\langle\psi_{K'}| + i|\psi_{K'}\rangle\langle\psi_K|, \quad (7c)$$

$$\tilde{\tau}_z = |\psi_K\rangle\langle\psi_K| - |\psi_{K'}\rangle\langle\psi_{K'}|, \quad (7d)$$

and s_0 is the unit matrix in spin space. The first term in Eq. (5), proportional to $\tilde{\tau}_0$, is just a simultaneous shift of the four energy levels. The second term in Eq. (5) is reminiscent of a Zeeman coupling Hamiltonian but here the roles of spin and the magnetic field are played by the valley operator $\tilde{\boldsymbol{\tau}}$ and the disorder-induced effective magnetic field $\boldsymbol{b}$, respectively.

In the presence of time-reversal (T) symmetry $b_z=0$ because in this case $T\psi_v$ is ψ_{-v} up to a phase factor, implying $|\Psi_\sigma^{(v)}(\boldsymbol{r}_{l\sigma})|^2=|\Psi_\sigma^{(-v)}(\boldsymbol{r}_{l\sigma})|^2$ and therefore $F_{l\sigma}^{(z)}=0$. In CNTs, in the case of moderate magnetic fields this statement still holds: an axial magnetic field induces an Aharonov-Bohm phase which does not modify the electronic wave functions (although induces energy shifts), and a perpendicular magnetic field interacts primarily with the spin of electrons via the Zeeman effect as long as the magnetic length is much larger than the nanotube radius. Therefore, throughout this paper we omit the b_z term from the effective disorder Hamiltonian $H_{\text{dis,eff}}$.

The remaining valley-Zeeman field $\boldsymbol{b}=(b_x,b_y,0)$ is random in the sense that it depends on the actual disorder con-

figuration. We consider some statistical properties of the valley-Zeeman field in the following. First, the averages of its components are

$$\langle b_{x,y}\rangle = \Omega_{\text{cell}} \sum_{l\sigma} \langle V_{l\sigma}\rangle F_{l\sigma}^{(x,y)} = 0. \tag{8}$$

Second, the variance of the components can be evaluated assuming that the envelope functions are "flat," i.e., $|\Psi_{\sigma}^{(v)}|^2 = 1/(\Omega_{\text{cell}}N)$, with N being the total number of carbon atoms in the QD. The result is $\langle b_{x,y}^2\rangle = \frac{\langle V_i^2\rangle}{2N}$. Furthermore, it can be proven that for large N, the quantities b_0, b_x, and b_y become statistically independent and characterized by Gaussian distributions, potentially facilitating future modeling of carbon-based QDs where disorder averaging is necessary.

Our results imply that the disorder-induced valley splittings in the quantum-dot energy spectrum should have an order of magnitude $\sqrt{\langle b_{x,y}^2\rangle}$. The typical on-site energy V_i on an impurity site is presumably on the atomic energy scale, therefore we take 1 eV as an estimate. Taking a quantum dot containing 10^5 atomic sites and 50 impurity sites we find the disorder-induced valley mixing energy scale $\sqrt{\langle b_{x,y}^2\rangle} \approx 50$ μeV, consistent with recent experiments carried out on CNT single and double quantum dots.[19,21]

It is important to note that the model presented in this section relies on the assumption that the disorder-induced valley-mixing energy scale is much smaller than the level spacing in the QD, i.e., the energy distance between the fourfold-degenerate level under consideration and its neighboring fourfold-degenerate levels. Recent measurements[19,21] imply that this assumption is reasonable in clean CNT QD devices. In the case when this assumption is invalid, i.e., if the valley-mixing energy scale becomes comparable to the level spacing, then valley mixing might become efficient *between* subsequent fourfold-degenerate levels, which implies that even the picture of independent fourfold-degenerate levels breaks down, let alone our model based on the concept of the valley-Zeeman field acting on a single fourfold-degenerate level. The mechanism that strong disorder mixes subsequent levels might actually be a reason for observing twofold (as opposed to fourfold) electron shell filling patterns in a number of CNT QD experiments.

For sake of completeness, we give the disorder-independent part of the single-electron Hamiltonian corresponding to a fourfold-degenerate QD energy level. The finite curvature of the CNT enhances spin-orbit interaction and leads to a significant splitting ($\Delta_{\text{SO}} \sim 100$ μeV) of the four levels.[19,51] Furthermore, an external magnetic field induces a Zeeman splitting of the spin states, and its axial component induces a splitting of the valley states as well. Therefore, the disorder-independent part of the Hamiltonian is

$$H_0 = -\frac{\Delta_{\text{SO}}}{2}\tilde{\tau}_z s_z + \mu_B \boldsymbol{B}\cdot\left(\frac{1}{2}g_s \boldsymbol{s} + \frac{1}{2}g_v \tilde{\tau}_z \hat{\boldsymbol{z}}\right), \tag{9}$$

where Δ_{SO} describes the energy splitting caused by the curvature-enhanced spin-orbit interaction, g_s and g_v are the spin and valley g factors, respectively, and $\hat{\boldsymbol{z}}$ is the unit vector in the z direction. The form of the Hamiltonian H_0 reflects the fact that at zero magnetic field, the Kramers theorem implies that the state pairs connected by time reversal, i.e., $(\psi_{K\uparrow}, \psi_{K'\downarrow})$ and $(\psi_{K\downarrow}, \psi_{K'\uparrow})$ are degenerate. In Fig. 2(b), we give an example for the evolution of a fourfold-degenerate level with magnetic field, which we obtain by diagonalizing $H_0 + H_{\text{dis,eff}}$ [cf. Eqs. (5) and (9)]. The parameters used for Fig. 2(b) are[19] $\Delta_{\text{SO}} = 370$ μeV, $\sqrt{b_x^2 + b_y^2} = 30$ μeV, $g_s = 2$, and $g_v = 54$. The valley-independent term proportional to b_0, which would shift the four levels simultaneously, is neglected.

To conclude this section: we have demonstrated that short-range disorder in CNT QDs appears as a random (in magnitude and direction) valley-Zeeman field in the effective Hamiltonian describing a fourfold- (spin and valley) degenerate quantum-dot level. We note that our derivation is not by any means specific to the particular geometry of nanotubes, and we expect the same qualitative consequences of short-range disorder in the case of electrostatically defined QDs in graphene[4] or silicon.[52–55]

III. TRANSPORT MODEL FOR A DOUBLE QUANTUM DOT

Our aim in this section is to provide a model for electronic transport through a few-electron CNT DQD which takes into account the following characteristic features of CNTs: (i) fourfold (spin and valley) degeneracy of the spectrum, (ii) spin-orbit interaction, and (iii) disorder-induced valley mixing. In the subsequent sections, we use this model to calculate the leakage current through a CNT DQD in the spin-valley blockade regime.

A. Hamiltonian

We use a constant-interaction Hamiltonian to model the few-electron CNT DQD. We take into account a single fourfold (spin and valley) energy level in each QD. We consider the case of spin- and valley-conserving interdot tunneling. We write the Hamiltonian in terms of creation $d_{Lvs}^{\dagger}$ ($d_{Rvs}^{\dagger}$) and annihilation d_{Lvs} (d_{Rvs}) operators of electrons on the left (right) dot having valley and spin quantum numbers v and s, respectively,

$$H_{\text{DQD}} = H_{\text{pot}} + H_{\text{e-e}} + H_{\text{so}} + H_{\text{dis}} + H_{\text{magn}} + H_{\text{tun}}, \tag{10a}$$

$$H_{\text{pot}} = \sum_{d=L,R} \epsilon_d n_d, \tag{10b}$$

$$H_{\text{e-e}} = \frac{U}{2}\sum_{d=L,R} n_d(n_d - 1) + U' n_L n_R, \tag{10c}$$

$$H_{\text{so}} = -\frac{\Delta_{\text{SO}}}{2}\sum_{d=L,R} s_{d,z}\tau_{d,z}, \tag{10d}$$

$$H_{\text{dis}} = \sum_{d=L,R} (b_{d,x}\tau_{d,x} + b_{d,y}\tau_{d,y}), \tag{10e}$$

$$H_{\text{magn}} = \mu_B \boldsymbol{B}\cdot\sum_{d=L,R}\left(\frac{1}{2}g_s \boldsymbol{s}_d + \frac{1}{2}g_v \tau_{d,z}\hat{\boldsymbol{z}}\right), \tag{10f}$$

$$H_{\text{tun}} = t\sum_{vs} d^{\dagger}_{Lvs} d_{Rvs} + \text{H.c.} \tag{10g}$$

The terms (10b)–(10g) in the Hamiltonian describe the effects of electrostatic potential difference between the dots, electron-electron interaction, spin-orbit coupling, short-range disorder, external magnetic field, and interdot tunneling, respectively. Here $d=L,R$ is the QD index, $n_{dvs}=d^{\dagger}_{dvs}d_{dvs}$, $n_d=\Sigma_{vs}n_{dvs}$, $\tau_{d,i}=\Sigma_{v,v',s}\tau_{i,vv'}d^{\dagger}_{dvs}d_{dv's}$, $s_{d,i}=\Sigma_{v,s,s'}s_{i,ss'}d^{\dagger}_{dvs}d_{dvs'}$, and both τ_i and s_i $(i=x,y,z)$ are the three Pauli matrices. Note that we have incorporated the valley-independent disorder-induced terms $\sim\tau_{L,0}$ and $\sim\tau_{R,0}$ into ϵ_L and ϵ_R, respectively. The operators $\tau_{d,k}$ $(d=L,R,\ k=0,x,y,z)$ defined above are the many-body generalizations of the single-particle operator $\tilde{\tau}_k$ defined in Eq. (7) but in Eq. (10) and henceforth we suppress the tilde for simplicity. We emphasize that the disorder-induced valley-Zeeman fields $\boldsymbol{b}_L=(b_{L,x},b_{L,y},0)$ and $\boldsymbol{b}_R=(b_{R,x},b_{R,y},0)$ are different in general, since the electrons on the left and right dot interact with a different set of impurities and therefore feel different disorder configurations. This feature is reminiscent of hyperfine interaction in conventional semiconductor DQDs, and will play a critical role in all the results we present in the forthcoming sections.

The system is in the spin-valley blockade regime if the available charge configurations for transport are the (1,1), (0,2), and (0,1) configurations (in general, these numbers might refer to the occupations in addition to completely filled shells, see below). In this situation, the only relevant parameter of $H_{\text{pot}}+H_{\text{e-e}}$ is the energy difference (or "detuning") Δ of (1,1) and (0,2) states: $\Delta=\epsilon_L-\epsilon_R+U'-U$. All results presented in this work correspond to zero detuning, $\Delta=0$, implying that the actual values of ϵ_L, ϵ_R, U, and U' do not affect our results. However, since in the following we neglect hybridization with (1,0) and (2,0), we implicitly assume that $t/(U-U')=t/(\epsilon_L-\epsilon_R)\ll 1$.

Motivated by the experiments we try to model here, we consider the case of an axial magnetic field: $\boldsymbol{B}=(0,0,B)$. In the CNT QD studied by Kuemmeth *et al.*[19] a spin g factor $g_s\approx 2$ and a valley g factor $g_v\sim 50$ have been found. However, the results we present in this work are insensitive to these values, because (at least in the parameter regimes under consideration here) (i) spin-Zeeman splitting do not affect the dynamics and (ii) we plot the magnetotransport curves against the field-induced valley splitting $\Delta_v=g_v\mu_B B$ and not against the field B itself.

Our constant-interaction approximation has the advantage of simplicity but also has the drawback that it does not account for the recently predicted Wigner-molecule formation effect.[7–9] This restricts the applicability of our model to (i) short quantum dots, where the confinement energy exceeds the interaction energy, or (ii) DQD systems where the environment (the metallic gate electrodes or the dielectric substrate, for example) provides a strong electrostatic screening and hence weakens the electron-electron interaction. Wigner-molecule formation implies a strong suppression of the supersinglet-supertriplet gap in the (0,2) charge configuration, which suppresses the Pauli blockade as well. The fact that Pauli blockade has been observed[20–22,29] in CNT DQDs indicates that the samples used in those experiments are closer to the constant-interaction regime than to the Wigner-molecule regime, which is a further motivation for us to use the constant-interaction model in our calculations.

Our Hamiltonian does not contain hyperfine interaction and spin- or valley-flip interdot tunneling matrix elements, although hyperfine interaction[43,44] and spin-orbit-induced spin-flip tunneling[45,46] have proven to be important in the understanding of spin blockade experiments in conventional semiconductor quantum dots. We neglect hyperfine interaction in this work because theoretical estimates indicate that its characteristic energy scale is below 5 neV even for fully ^{13}C-enriched samples[6,10,47]), being small compared to other relevant energy scales in our system i.e., spin-orbit splitting $\gtrsim 100$ μeV, disorder $\gtrsim 10$ μeV, interdot tunneling, and valley splitting $\gtrsim$ μeV, see forthcoming sections. Note that recent experiments[21,22] indicate a two orders of magnitude larger hyperfine energy scale than the theoretical estimates, and therefore we cannot be conclusive about the relevance of this effect. Experiments in GaAs and CNT DQDs have shown that hyperfine coupling becomes especially relevant at suppressed interdot tunneling or large detuning, therefore our model excluding this mechanism might not be adequate in that regime.

Spin-orbit-induced spin-flip interdot tunneling could in principle be present in our system, but only between states having a ± 1 difference in their circumferential quantum number, as it can be deduced from Eqs. (31)–(33) of Ref. 5. This possibility is not ruled out in some of the spin-valley blockade transport experiments[22] as those were not performed in the actual (1,1)-(0,2)-(0,1) regime (which would imply that in both dots the electrons occupy the lowest-energy circumferential mode of the CNT and therefore spin-flip tunneling is forbidden). For example, in the $(4n+1,4m+1)-(4n,4m+2)-(4n,4m+1)$ regime the spin-valley blockade could take place "on top of" $n(m)$ filled shells in the left (right) dot. However, we postpone the analysis of spin-flip tunneling for future work and in Sec. IV we demonstrate that agreement with experimental results can be obtained from our model even though spin-flip tunneling is not taken into account.

B. Generalized master equation

We apply the master-equation formalism to describe the transport process through the serially coupled DQD system. The DQD charge configurations which are relevant for the transport process considered here are the (1,1), (0,2), and (0,1) configurations. Hence the state of the DQD system is described by the 26×26 density matrix ρ, where the Hilbert space is spanned by 16 states in the (1,1) charge configuration, six states in the (0,2) charge configuration, and four states in the (0,1) configuration. The time dependence of ρ is governed by the generalized master equation or Lindblad equation

$$\dot{\rho} = -\frac{i}{\hbar}[H_{\text{DQD}},\rho] + D\rho. \tag{11}$$

The dissipative term $D\rho$ describes the tunneling events to and from the DQD, characterized by the rates Γ_L and Γ_R, respectively. It has the following form:

$$D\rho = \Gamma_L \sum_{vs} \left(d^\dagger_{Lvs}\rho d_{Lvs} - \frac{1}{2}\rho d_{Lvs}d^\dagger_{Lvs} - \frac{1}{2} d_{Lvs}d^\dagger_{Lvs}\rho \right) + \Gamma_R \sum_{vs} \left(d_{Rvs}\rho d^\dagger_{Rvs} - \frac{1}{2}\rho d^\dagger_{Rvs}d_{Rvs} - \frac{1}{2} d^\dagger_{Rvs}d_{Rvs}\rho \right). \tag{12}$$

Here the creation and annihilation operators are restricted to the charge configurations participating in the transport process.

C. Secular approximation

We assume that the splittings between the eigenvalues of H_{DQD} are larger than the level broadenings set by the tunneling energies $h\Gamma_L$ and $h\Gamma_R$. This allows us to use the so-called secular approximation,[56] i.e., to assume that the steady-state density matrix is diagonal in the eigenbasis of H_{DQD}. Hence the generalized master equation simplifies to a steady-state classical master equation (CME),

$$0 = \dot{\rho}_\alpha = -\rho_\alpha \Gamma_R \sum_j p_{j\alpha} + \Gamma_L \sum_j \rho_j r_{\alpha j}, \tag{13a}$$

$$0 = \dot{\rho}_i = -\rho_i \Gamma_L \sum_\beta r_{\beta i} + \Gamma_R \sum_\beta \rho_\beta p_{i\beta}. \tag{13b}$$

Here $\alpha,\beta=1,\ldots,22$ $(i,j=1,2,3,4)$ refers to the two-electron (single-electron) DQD energy eigenstates, $\rho_\alpha=\rho_{\alpha\alpha}$ and $\rho_i=\rho_{ii}$, and

$$r_{\alpha i} = \sum_{vs} |\langle i|d_{Lvs}|\alpha\rangle|^2, \tag{14a}$$

$$p_{i\alpha} = \sum_{vs} |\langle i|d_{Rvs}|\alpha\rangle|^2. \tag{14b}$$

D. Eliminating (0,1) states from the classical master equation

The Hamiltonian has a block-diagonal structure: the two-electron [(1,1) and (0,2)] and single-electron (0,1) blocks are uncoupled. However, the Lindblad terms do couple these sectors because they describe single-electron tunneling onto and from the DQD. The coupling is appearing in the CME in the form of the rates $\Gamma_L r_{\alpha i}$ and $\Gamma_R p_{i\alpha}$.

Throughout this analysis, we consider the case $\Gamma_L \gg \Gamma_R$. The reason is that in the spin-valley blockade regime the characteristic scale of the rates $\Gamma_L r_{\alpha i}$ are largely independent of the spin and valley physics inside the DQD, whereas the rates $\Gamma_R p_{i\alpha}$ are sensitive to those, so in order to have the transport via the DQD sensitive to spin and valley effects, the outgoing rates $\Gamma_R p_{i\alpha}$ should provide the transport bottleneck.

We claim that in this limit $\Gamma_R/\Gamma_L \to 0$, the steady-state CME is reduced to a homogeneous linear set of equations $M\rho=0$ for the vector $\rho=(\rho_1,\rho_2,\ldots,\rho_{22})$ which contains the diagonal elements of the two-electron sector of the DQD density matrix ρ, and the normalization condition $\Sigma_\alpha \rho_\alpha = 1$. The coefficient matrix M is given as

$$M_{\alpha\beta} = \sum_j \left(\frac{r_{\alpha j} p_{j\beta}}{\sum_\gamma r_{\gamma j}} - \delta_{\alpha\beta} p_{j\alpha} \right). \tag{15}$$

The proof of this statement is a straightforward calculation starting from the steady-state CME in Eq. (13).

Having the steady-state occupation probabilities ρ_α and the corresponding energy eigenstates $|\alpha\rangle$ at hand, we calculate the current as the average decay rate of the two-electron states with respect to the steady-state distribution,

$$I = e\Gamma_R \sum_\alpha \rho_\alpha \sum_j p_{j\alpha}. \tag{16}$$

IV. STRONG SPIN-ORBIT COUPLING

In this section, we describe the spin-valley blockade effect in a CNT DQD in the case when spin-orbit coupling dominates the energy spectrum over disorder, interdot tunneling, and magnetic-field-induced spin and valley splitting, i.e., $\Delta_{\mathrm{SO}} \gg b, t, \Delta_v, \Delta_s$. Here b denotes the typical energy scale of the disorder-induced valley-Zeeman fields on the two dots. The main result of this section is that we identify a parameter regime ($t \lesssim \frac{b_-^2}{\Delta_{\mathrm{SO}}}$, where $b_-^2 = b_L^2 - b_R^2$) where the current as the function of magnetic field (the "magnetotransport curve") shows a dip around zero field, and the width of the dip is controllable by the interdot tunneling amplitude t. This field-induced increase in the current is in qualitative agreement with experiments.[21,22] We interpret this result using Löwdin perturbation theory,[57] and provide an analytical formula for the current which can be well fitted to the numerical results using a single fitting parameter, the average number of transmitted electrons between two blocking events.[58] In the following, we describe the case $t \sim \frac{b_-^2}{\Delta_{\mathrm{SO}}}$. In Appendix A, we argue that the findings of this regime can be extended to the regime $t \ll \frac{b_-^2}{\Delta_{\mathrm{SO}}}$ as well, and in Appendix B we show that they do not hold if $t \gg \frac{b_-^2}{\Delta_{\mathrm{SO}}}$.

We start our analysis by presenting the numerical results for this regime. In Fig. 3, we show the current as a function of the magnetic-field-induced valley splitting Δ_v, for a fixed value of spin-orbit coupling Δ_{SO} and disorder-induced valley fields $\boldsymbol{b}_L$ and $\boldsymbol{b}_R$ (see caption) but different values of interdot tunneling t. All parameters have a realistic order of magnitude.[19,21] (Note that the Zeeman spin splitting Δ_s plays no role in the transport process, see below.) In qualitative agreement with recent experiments,[21,22] the data in Fig. 3 shows a zero-field dip in the current, and the width of the dip is controlled by the interdot tunneling t. In all the three cases displayed, the ratio of the zero-field current $I_0 \equiv I(B=0)$ and the maximal current $I_{\max}$ is $I_{\max}/I_0 \approx 1.5$. This ratio agrees well with that observed experimentally in Ref. 21 [see Fig. 3(a) therein], however, in Ref. 22 a ratio of $I_{\max}/I_0 \sim 50$ has been found [see Fig. 3(e) therein]. Below we argue that the

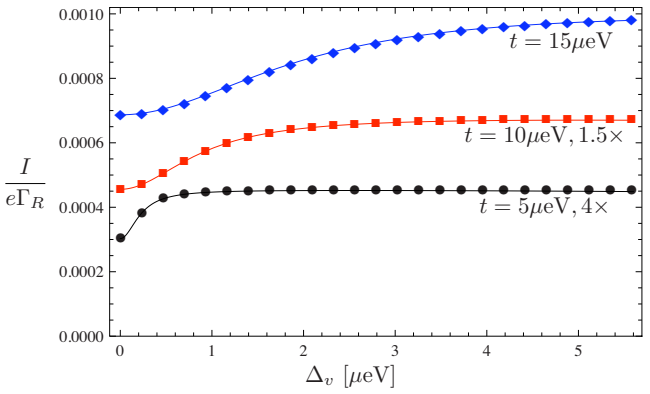

FIG. 3. (Color online) Numerical results for the current as a function of magnetic-field-induced valley splitting for different values of interdot tunneling (shown). Further parameters: $\Delta_{SO}=250$ μeV, $b_{Lx}=20$ μeV, $b_{Ly}=10$ μeV, $b_{Rx}=80$ μeV, $b_{Ry}=0$ μeV, and therefore $b_-^2/\Delta_{SO}=23.6$. Points: numerical data. Curves: the analytical formula (23) fitted to the numerical data with n^* as the single fitting parameter. Lower two data sets are scaled as shown.

factor $I_{max}/I_0 \approx 1.5$ we deduce from Fig. 3 is a rough upper bound for this quantity in the parameter regime under consideration, and therefore we conclude that our results (i) agree very well with the measurement of Ref. 21, and (ii) match the measurement of Ref. 22 only qualitatively, which might be due to mechanisms missing from our model or sample parameters in the experiment not fitting into the parameter regime we consider here. Further discussion on this discrepancy with Ref. 22 is provided in Sec. VI. In the remaining part of this section, we provide an interpretation of the numerical results shown in Fig. 3 and derive an analytical formula for the current using Löwdin perturbation theory.

The transition rates in the classical master equation [Eq. (13)] are determined by the eigenstates of the two-electron Hamiltonian. To provide an interpretation of the numerical results, we will describe those energy eigenstates using perturbation theory. We start with the two-electron Fock basis based on the single-particle states $\psi_{K\uparrow}$, $\psi_{K'\downarrow}$ and $\psi_{K\downarrow}$, $\psi_{K'\uparrow}$ [the pairs are energetically separated by the spin-orbit energy Δ_{SO} at zero field, see Eq. (9)]. The (1,1) states are denoted in the form $|K\uparrow, K'\uparrow\rangle$ whereas the (0,2) states in the form $|0, K\uparrow K'\uparrow\rangle$. We perform a basis transformation in order to obtain basis states which are eigenstates of the two-electron spin-orbit Hamiltonian [Eq. (10d)] and have well-defined supersinglet or supertriplet character at the same time. This new basis is presented in Table I, classified according to their properties outlined below. This basis will serve as the set of unperturbed states in our perturbation calculations.

An important simplifying observation is that even in the presence of spin-orbit coupling and a magnetic field parallel to the nanotube axis, the axial component of the electron spin S_z is conserved. This allows us to separate the 22 states of the two-electron basis to three uncoupled spin subspaces (see columns in Table I): five states which are spin polarized with a polarization aligned with the z axis (up-spin states), five states which are spin polarized with a polarization antialigned with the z axis (down-spin states), and 12 states having mixed spin states. As the three different spin subspaces shown in the columns of Table I are not coupled by any terms in the Hamiltonian, the Zeeman spin splitting Δ_s plays no role in the transport process. Besides their spin state, our unperturbed states can also be classified according to their spin-orbit energy. Five (five) of those have a spin-orbit energy Δ_{SO} ($-\Delta_{SO}$), and 12 have a vanishing spin-orbit energy (see rows in Table I).

To visualize the matrix elements of the Hamiltonian, in Fig. 4 we show the level diagram of the unperturbed basis states we introduced in Table I. The horizontal arrangement of the states reflects the charge configuration, and the vertical arrangement reflects the spin-orbit energies. Red/gray lines denote supertriplet states and black lines denote supersinglet states. The green/light gray (blue/dark gray) arrows correspond to off-diagonal elements of the Hamiltonian in this basis, induced by disorder (interdot tunneling).

In the polarized spin subspaces [Fig. 4(a)], the high- and low-energy (1,1) states [dashed lines in Fig. 4(a)] are coupled to the (0,2) state via disorder and tunneling, resulting in a small decay rate at small fields ($\Delta_v \ll \Delta_{SO}$),

$$\Gamma_{s,\pm} = \Gamma_s \left(1 \mp 2\frac{\Delta_v}{\Delta_{SO}}\right)^{-4}, \tag{17}$$

where the $\pm$ sign refers to the up-spin and down-spin subspaces, respectively, $\Gamma_s = \frac{t^2 b_a^2}{\Delta_{SO}^4}\Gamma_R \ll \Gamma_R$ and $\boldsymbol{b}_a = \boldsymbol{b}_L - \boldsymbol{b}_R$. Here

TABLE I. The 22 basis states used for perturbation calculations in the presence of strong spin-orbit coupling. The six (1,1) states involving a minus sign are supersinglets, the ten further (1,1) states are supertriplets. The six (0,2) states are supersinglets.

Spin-orbit energy	Up-spin ($S_z=+1$)	Down-spin ($S_z=-1$)	Mixed spin ($S_z=0$)
Δ_{SO}	$\|K'\uparrow, K'\uparrow\rangle$	$\|K\downarrow, K\downarrow\rangle$	$\frac{1}{\sqrt{2}}(\|K\downarrow, K'\uparrow\rangle \pm \|K'\uparrow, K\downarrow\rangle)$ $\|0, K\downarrow K'\uparrow\rangle$
0	$\frac{1}{\sqrt{2}}(\|K\uparrow, K'\uparrow\rangle \pm \|K'\uparrow, K\uparrow\rangle)$ $\|0, K\uparrow K'\uparrow\rangle$	$\frac{1}{\sqrt{2}}(\|K\downarrow, K'\downarrow\rangle \pm \|K'\downarrow, K\downarrow\rangle)$ $\|0, K\downarrow K'\downarrow\rangle$	$\frac{1}{\sqrt{2}}(\|K\uparrow, K\downarrow\rangle \pm \|K\downarrow, K\uparrow\rangle)$ $\|0, K\uparrow K\downarrow\rangle$ $\frac{1}{\sqrt{2}}(\|K'\uparrow, K'\downarrow\rangle \pm \|K'\downarrow, K'\uparrow\rangle)$ $\|0, K'\uparrow K'\downarrow\rangle$
$-\Delta_{SO}$	$\|K\uparrow, K\uparrow\rangle$	$\|K'\downarrow, K'\downarrow\rangle$	$\frac{1}{\sqrt{2}}(\|K\uparrow, K'\downarrow\rangle \pm \|K'\downarrow, K\uparrow\rangle)$ $\|0, K\uparrow K'\downarrow\rangle$

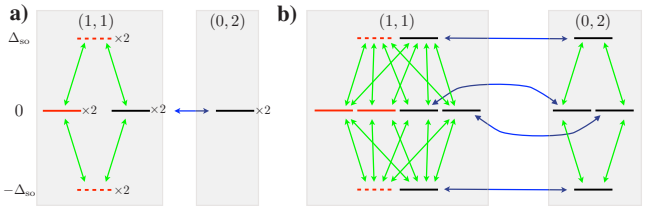

FIG. 4. (Color online) Unperturbed two-electron states (lines) and their energies in a CNT DQD at strong spin-orbit coupling and zero magnetic field (cf. Table I). Horizontal arrangement of the states reflects charge configuration and vertical arrangement reflects spin-orbit energies. Red/gray lines: supertriplet states. Dashed red/gray lines: blocked supertriplet states. Black lines: supersinglet states. Green/light gray (blue/dark gray) arrows correspond to off-diagonal elements of the Hamiltonian, induced by disorder (interdot tunneling). (a) Up-spin and down-spin states. The indicated ×2 degeneracy corresponds to the two possible spin configurations. Different spin species are uncoupled. (b) Mixed-spin states.

and hereafter the decay rate of a two-electron state α is meant to be the sum of the four transition rates into the four different (0,1) single-electron states, i.e., $\Sigma_{j=1}^{4} p_{j\alpha}$. In the up-spin (down-spin) subspace the decay rate increases (decreases) as the magnetic field increases because the magnetic field pushes the high- and low-energy states closer to (away from) the zero-energy (1,1) and (0,2) states, cf. Eq. (10f). The decay rate Γ_s is fourth order in small parameters, therefore we call these four states (i.e., the high- and low-energy up-spin and down-spin states) "blocked."

To describe the energy eigenstates in the spin-polarized zero-energy subspace, conventional degenerate perturbation theory is not applicable since the perturbative hybridization of the (1,1) supertriplet state with the (1,1) supersinglet would include a zero-energy denominator. Therefore, we apply Löwdin perturbation theory[59] to derive an effective Hamiltonian for the zero-energy spin-polarized subspace. At zero field, we obtain

$$H_{0,\pm} = \begin{pmatrix} 0 & \mp\frac{b_-^2}{\Delta_{\mathrm{SO}}} & 0 \\ \mp\frac{b_-^2}{\Delta_{\mathrm{SO}}} & 0 & \sqrt{2}t \\ 0 & \sqrt{2}t & 0 \end{pmatrix}. \tag{18}$$

In $H_{0,\pm}$, the first index refers to the zero-energy subspace and $\pm$ to the up-spin and down-spin subspaces. The effective Hamiltonian $H_{0,\pm}$ corresponds to the following ordering of the basis states: (1,1) supertriplet, (1,1) supersinglet, (0,2) supersinglet. Remarkably, $H_{0,\pm}$ is independent of the angle between the two disorder-induced valley fields in the double dot. From Eq. (18) and our assumption $\frac{b_-^2}{\Delta_{\mathrm{SO}}} \sim t$, it follows that the three basis states are completely mixed, and each of them acquires a decay rate $\sim\Gamma_R$. Therefore with respect to the spin-polarized subspaces, we conclude that in the regime considered in this section, the ten energy eigenstates can be divided to a set of four blocked states decaying with slow rates $\Gamma_{s,\pm} \ll \Gamma_R$, and six unblocked states which decay orders-of-magnitude faster (with rates $\sim\Gamma_R$) than the blocked ones.

Now we extend this analysis to the 12-dimensional mixed-spin subspace [Fig. 4(b)]. In the high- and low-energy mixed spin subspaces the effective Hamiltonian, we obtain is (common diagonal elements are omitted),

$$H_{\pm,0} = \begin{pmatrix} 0 & -\frac{2b_-^2\Delta_v}{\Delta_{\mathrm{SO}}^2 - 4\Delta_v^2} & 0 \\ -\frac{2b_-^2\Delta_v}{\Delta_{\mathrm{SO}}^2 - 4\Delta_v^2} & 0 & \sqrt{2}t \\ 0 & \sqrt{2}t & \mp\frac{b_-^2\Delta_{\mathrm{SO}}}{\Delta_{\mathrm{SO}}^2 - 4\Delta_v^2} \end{pmatrix}. \tag{19}$$

Here the ordering of states is analogous to that in Eq. (18), and the first index of $H_{\pm,0}$ refers to the high- or low-energy subspace whereas the second index refers to the mixed spin subspace. At zero field, the valley splitting is $\Delta_v = 0$, implying that the first basis state, i.e., the (1,1) supertriplet is uncoupled from the other two states, in particular, from the (0,2) supersinglet. Therefore, at zero field the high- or low-energy (1,1) supertriplet state [dashed lines in Fig. 4(b)] can decay only due to its perturbative coupling (via disorder and tunneling) to the two zero-energy (0,2) supersinglets. From Löwdin theory, we infer that the decay rate of the high- and low-energy (1,1) supertriplets due to these processes is

$$\Gamma_{s,0} = \frac{1}{2}(\Gamma_{s,+} + \Gamma_{s,-}), \tag{20}$$

and therefore these two states are blocked in the sense defined above. However, according to Eq. (19), a finite valley splitting Δ_v induces mixing between the two (1,1) states. This mixing provides an additional decay channel for the (1,1) supertriplet state with a rate

$$\Gamma_c = \frac{2b_-^4\Delta_v^2}{t^2(\Delta_{\mathrm{SO}}^2 - 4\Delta_v^2)^2}\Gamma_R, \tag{21}$$

inferred using standard perturbation theory in the field-induced coupling term. This rate becomes much faster than the slow rate $\Gamma_{s,0}$ if the field is strong enough to ensure $\Delta_v > \frac{t^2 b_a}{\sqrt{2}b_-^2}$. In conclusion, we have found that in both the high- and low-energy mixed spin subspace the total decay rate of the (1,1) supertriplet state $\Gamma_{s,0}+\Gamma_c$ changes dramatically as the magnetic field is turned on: at zero field these two states are blocked, having the slow decay rate $\Gamma_{s,0}$ whereas at finite field their decay rate grows with orders of magnitudes.

In the six-dimensional zero-energy mixed spin subspace, the order of magnitude of the decay rates is not influenced by the magnetic field. Each of these states decay fast compared to the slow rate Γ_s. This can be derived in the same way as shown at the discussion of the zero-energy spin-polarized subspace and Eq. (18).

Using the explicitly calculated decay rates, we can set up a semiphenomenological analytical formula for the current. To this end, we regard the transport process as an alternation of charge transfer "bursts" (subsequent occupation of unblocked states) and blocking events (due to occupying one of the blocked states). We assume that a burst corresponds to a

transfer of n^* electrons on average, i.e., n^* is not necessarily integer.[58] Since the charge bursts happen fast compared to the time spent in a blocked state, the average time between two subsequent bursts can be estimated as the average of the decay times of the six blocked states, i.e.,

$$T_{\text{burst}} \approx \frac{1}{6}[2\Gamma_{s,+}^{-1} + 2\Gamma_{s,-}^{-1} + 2(\Gamma_{s,0} + \Gamma_c)^{-1}]. \tag{22}$$

As a burst transfers n^* electrons on average, the current can be expressed as

$$I \approx \frac{en^*}{T_{\text{burst}}}. \tag{23}$$

Equation (23), together with Eq. (22) and the decay rates calculated above, provides an analytical expression for the current as a function of the parameters of the Hamiltonian and Γ_R, having a single phenomenological parameter n^*. We have fitted this analytical result using n^* as the single fitting parameter to our numerical results (Fig. 3), and we have found $n^* \approx 3.2$ irrespective of the value of tunneling amplitude t. As seen in Fig. 3, this value of n^* gives an excellent agreement between our numerical and analytical results in the considered range of magnetic field. By repeating the numerical calculations and the fittings for various disorder configurations we generally find good agreement between numerics and analytics. The values we obtain for n^* are typically between 1.4 and 5.2, indicating that n^* is not universal but depends on the details of the Hamiltonian.

Our analytical result for the current enables us to qualitatively explain two characteristic features of the magnetotransport curves shown in Fig. 3. One of those features is the ratio $I_{\max}/I_0 \approx 1.5$. Evaluating the current according to Eq. (23) at zero field, we find $I_0 = en^*\Gamma_s$, whereas at high field, where $\Gamma_c \gg \Gamma_s$, we can neglect $(\Gamma_{s,0}+\Gamma_c)^{-1}$ in Eq. (22) and find $I_{\max} \approx en^* 6\Gamma_s/4$, resulting in the ratio $I_{\max}/I_0 \approx 1.5$, in correspondence with our numerical results in Fig. 3 and the experimental data of Ref. 21. For this estimate we neglected the field dependence of the rates $\Gamma_{s,\pm}$ but taking that into account could only lower the ratio $I_{\max}/I_0$. A second feature observed in Fig. 3 is that the width of the zero-field dip of the magnetotransport curve depends on the tunneling amplitude t. This is explained by the fact that the crossing-over rate in Eq. (21) depends on the tunneling amplitude as $\Gamma_c \propto 1/t^2$, i.e., the stronger the tunneling, the "slower" the crossover of Γ_c as the magnetic field increases, and therefore the wider the zero-field dip in the magnetotransport data. In Appendix A we argue that the conclusions drawn in this section for the case $t \sim \frac{b_z^2}{\Delta_{\text{SO}}}$ can be generalized to the regime $t \ll \frac{b_z^2}{\Delta_{\text{SO}}}$, and therefore the range of validity of our results is actually $t \lesssim \frac{b_z^2}{\Delta_{\text{SO}}}$.

Finally we point out a possible generalization of our results. In the system under consideration, the spin and valley degrees of freedom play a symmetric role in the absence of disorder and magnetic field, since the spin-orbit Hamiltonian $H_{\text{so}} \propto s_z\tau_z$ is symmetric in spin and valley, and the interdot tunneling conserves both spin and valley. The results of this section show that if disorder provides an inhomogeneous valley-Zeeman field (coupled to τ_x and τ_y) in the DQD, then the dynamics becomes independent of the spin-Zeeman splitting, and the magnetotransport curve shows a dip at zero axial magnetic field. These results can be transferred to the case when the role of spin and valley are exchanged: in the hypothetic case of absence of disorder, an inhomogeneous spin-Zeeman field, coupled to s_x and s_y but not to s_z, e.g., coming from a perpendicular-to-nanotube-axis magnetic field, would imply that the dynamics becomes independent of the valley-Zeeman splitting, and the magnetotransport curve would show a dip at zero axial magnetic field.

To conclude this section, solving the transport master equation numerically, we have found that if $\Delta_{\text{SO}} \gg \frac{b_z^2}{\Delta_{\text{SO}}} \gtrsim t$ and $\Delta_{\text{SO}} \gg \Delta_v$, then the magnetotransport curves show a zero-field dip with a width that is controllable by the interdot tunneling amplitude t, in agreement with a recent experiment.[22] Using Löwdin perturbation theory, we gave an analytical formula for the current and based on that, a qualitative interpretation of the features of our numerical results. We emphasize that the observed characteristic magnetotransport pattern is due to the different disorder-induced effective valley-Zeeman fields on the two quantum dots. Our theory predicts a typical ratio of the finite-field and zero-field currents $I_{\max}/I_0 \lesssim 1.5$, which is in line with the experimental result of Ref. 21, but different from that of Ref. 22, possibly due to experimental sample parameters not fitting into the parameter range studied here or mechanisms missing from our transport model.

V. STRONG DISORDER

In this section, we describe the spin-valley blockade effect in a CNT DQD in the case of strong disorder, weak interdot tunneling and weak spin-orbit coupling ($b \gg t, \Delta_{\text{SO}}$). In recent experiments on clean nanotube QDs, the spin-orbit splitting of the fourfold-degenerate ground-state energy level has been found significantly larger than the valley mixing energy scale. However, in nanotubes with stronger impurity contamination (larger radius) the disorder (spin-orbit interaction) energy scale is expected to increase (decrease), and the regime considered in this section might be reached. A further motivation to study this regime is its possible relevance for certain silicon-[52–55] or graphene-based quantum dots.[4] In those material systems, the spin-orbit interaction is expected to be smaller than in CNTs but short-range disorder couples valleys for the same reason as it does in CNTs.

As the main result of this section, we show that in the parameter regime under consideration, the magnetotransport curve shows a zero-field dip or peak depending on the disorder configuration. We find that at a given value of the external magnetic field, the current is determined by three parameters (if interdot tunneling t and emptying rate Γ_R are fixed): the angle $\theta^{(\text{tot})}$ between the two total valley-Zeeman fields $\boldsymbol{b}_L^{(\text{tot})} \equiv \boldsymbol{b}_L + \Delta_v\hat{\boldsymbol{z}}/2$ and $\boldsymbol{b}_R^{(\text{tot})} \equiv \boldsymbol{b}_R + \Delta_v\hat{\boldsymbol{z}}/2$ on the two dots, and the lengths of these valley-Zeeman fields $b_L^{(\text{tot})}$ and $b_R^{(\text{tot})}$. Our analysis is analogous to the derivation of the spin blockade leakage current induced by hyperfine interaction in GaAs double dots,[44] with the most important difference being that in our case spin-independent disorder provides a

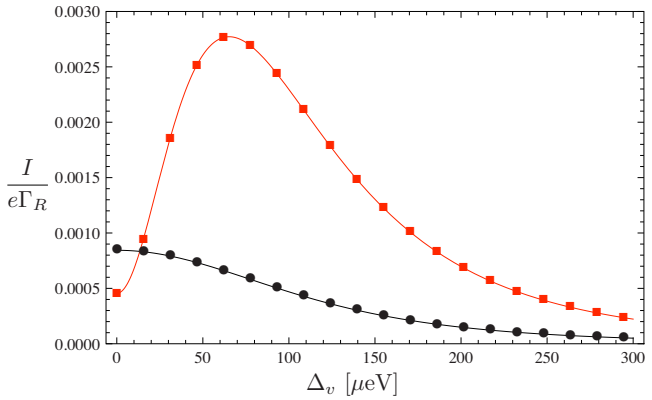

FIG. 5. (Color online) Numerical (dots) and analytical (lines) results for the current as a function of magnetic-field-induced valley splitting for two different disorder realizations. Parameters: $t=10$ μeV, $b_{Lx}=\cos\theta\times 100$ μeV, $b_{Ly}=\sin\theta\times 100$ μeV, $b_{Rx}=200$ μeV, and $b_{Ry}=0$ μeV. Circles: $\theta=\pi/4$. Boxes: $\theta=15\pi/16$.

blockade-lifting mechanism via the valley dynamics, whereas in conventional spin blockade, the hyperfine interaction affecting spin dynamics is responsible for lifting the blockade.

We start our analysis by presenting numerical results in Fig. 5. The figure shows the magnetic-field dependence of the current for two different disorder realizations. The two curves are qualitatively different: one shows a zero-field dip whereas the other shows a zero-field peak. In the following, using standard perturbation theory and an approximative analytical solution of the master equation we show that the qualitative difference between the two curves is related to the fact that the angle θ between the disorder-induced valley-Zeeman fields on the two dot differs for the two disorder realizations.

We exploit the fact that the full Hamiltonian commutes with the axial (z) component of the electron spin, and therefore one can identify four uncoupled spin subspaces of the 22-dimensional two-electron Hilbert space. It is beneficial to choose a classification corresponding to the standard two-electron spin-singlet and spin-triplet states $|S\rangle_s$, $|T_+\rangle_s$, $|T_0\rangle_s$, and $|T_-\rangle_s$ (the outer lower index refers to "spin"). Since these four spin subspaces are uncoupled from each other, the spin-Zeeman effect has no effect on the dynamics and therefore from now on we disregard that.

In the absence of interdot tunneling, the energy eigenstates of the single-electron Hamiltonian are trivial: in the left dot they are $|K_L\uparrow\rangle$, $|K_L\downarrow\rangle$, $|K'_L\uparrow\rangle$, and $|K'_L\downarrow\rangle$, where $|K_L\rangle$ and $|K'_L\rangle$ are defined as the eigenstates of the 2×2 matrix $\boldsymbol{b}_L^{(\mathrm{tot})}\cdot\boldsymbol{\tau}$ corresponding to the eigenvalue $b_L^{(\mathrm{tot})}$ and $-b_L^{(\mathrm{tot})}$, respectively. Single-electron energy eigenstates of the right dot are constructed accordingly. The two-electron energy eigenstates are the standard Fock basis states constructed from these single-electron states (as long as interdot tunneling is zero). The resulting 22 energy eigenstates are classified regarding their energy eigenvalue and spin state in Table II.

At this point, we make use of the fact that the magnitudes of the total valley-Zeeman fields in the two dots are typically different (since they have a random contribution induced by the random arrangement of disorder), and their difference is typically comparable to themselves

$$b_L^{(\mathrm{tot})} \sim b_R^{(\mathrm{tot})} \sim b_L^{(\mathrm{tot})} - b_R^{(\mathrm{tot})}. \tag{24}$$

Note that this condition can hold only if the magnetic-field-induced valley-Zeeman field Δ_v does not dominate over the disorder-induced component, which restricts the validity of the following analysis to the range $\Delta_v \lesssim b$. If the condition (24) holds, then the separations between the seven energy levels considered in Table II are on the order of b, which is much larger than the interdot tunneling t, and therefore we are allowed to treat t as a perturbation, and use the states listed in Table II as the unperturbed states.

Due to tunneling, the (1,1) states (upper four rows in Table II) perturbatively hybridize with (0,2) states (lower three rows in Table II) and therefore acquire a finite decay rate. As shown in Table II and Fig. 6(a), in each of the three spin-triplet subspaces there are four (1,1) states and they hybridize with a single available (0,2) state. Standard perturbation theory and Eq. (14b) gives two different decay rates,

$$\frac{\Gamma_{1T}}{\Gamma_R} = \frac{2t^2\cos^2(\theta^{(\mathrm{tot})}/2)}{(b_L^{(\mathrm{tot})} - b_R^{(\mathrm{tot})})^2}, \tag{25a}$$

$$\frac{\Gamma_{2T}}{\Gamma_R} = \frac{2t^2\sin^2(\theta^{(\mathrm{tot})}/2)}{(b_L^{(\mathrm{tot})} + b_R^{(\mathrm{tot})})^2}. \tag{25b}$$

The rate Γ_{1T} (Γ_{2T}) corresponds to the spin-triplet states in the second and third (first and fourth) lines of Table II. In the spin-singlet subspace, there are three (0,2) states to hybridize

TABLE II. The 22 basis states used for perturbation calculations in the presence of strong disorder. Different columns correspond to different spin states and each row has a corresponding energy (left column; spin Zeeman energies are neglected). The upper four [lower three] rows contain the (1,1) states [(0,2) states].

Energy	$\lvert S\rangle_s$	$\lvert T_+\rangle_s$	$\lvert T_0\rangle_s$	$\lvert T_-\rangle_s$
$b_L^{(\mathrm{tot})}+b_R^{(\mathrm{tot})}$	$\frac{1}{\sqrt{2}}(\lvert K_L\uparrow,K_R\downarrow\rangle-\lvert K_L\downarrow,K_R\uparrow\rangle)$	$\lvert K_L\uparrow,K_R\uparrow\rangle$	$\frac{1}{\sqrt{2}}(\lvert K_L\uparrow,K_R\downarrow\rangle+\lvert K_L\downarrow,K_R\uparrow\rangle)$	$\lvert K_L\downarrow,K_R\downarrow\rangle$
$-b_L^{(\mathrm{tot})}+b_R^{(\mathrm{tot})}$	$\frac{1}{\sqrt{2}}(\lvert K'_L\uparrow,K_R\downarrow\rangle-\lvert K'_L\downarrow,K_R\uparrow\rangle)$	$\lvert K'_L\uparrow,K_R\uparrow\rangle$	$\frac{1}{\sqrt{2}}(\lvert K'_L\uparrow,K_R\downarrow\rangle+\lvert K'_L\downarrow,K_R\uparrow\rangle)$	$\lvert K'_L\downarrow,K_R\downarrow\rangle$
$b_L^{(\mathrm{tot})}-b_R^{(\mathrm{tot})}$	$\frac{1}{\sqrt{2}}(\lvert K_L\uparrow,K'_R\downarrow\rangle-\lvert K_L\downarrow,K'_R\uparrow\rangle)$	$\lvert K_L\uparrow,K'_R\uparrow\rangle$	$\frac{1}{\sqrt{2}}(\lvert K_L\uparrow,K'_R\downarrow\rangle+\lvert K_L\downarrow,K'_R\uparrow\rangle)$	$\lvert K_L\downarrow,K'_R\downarrow\rangle$
$-b_L^{(\mathrm{tot})}-b_R^{(\mathrm{tot})}$	$\frac{1}{\sqrt{2}}(\lvert K'_L\uparrow,K'_R\downarrow\rangle-\lvert K'_L\downarrow,K'_R\uparrow\rangle)$	$\lvert K'_L\uparrow,K'_R\uparrow\rangle$	$\frac{1}{\sqrt{2}}(\lvert K'_L\uparrow,K'_R\downarrow\rangle+\lvert K'_L\downarrow,K'_R\uparrow\rangle)$	$\lvert K'_L\downarrow,K'_R\downarrow\rangle$
$2b_R^{(\mathrm{tot})}$	$\lvert 0,K_R\uparrow K_R\downarrow\rangle$	$\lvert 0,K_R\uparrow K'_R\uparrow\rangle$	$\frac{1}{\sqrt{2}}(\lvert 0,K_R\uparrow K'_R\downarrow\rangle+\lvert 0,K_R\downarrow K'_R\uparrow\rangle)$	$\lvert 0,K_R\downarrow K'_R\downarrow\rangle$
0	$\frac{1}{\sqrt{2}}(\lvert 0,K_R\uparrow K'_R\downarrow\rangle-\lvert 0,K_R\downarrow K'_R\uparrow\rangle)$			
$-2b_R^{(\mathrm{tot})}$	$\lvert 0,K'_R\uparrow K'_R\downarrow\rangle$			

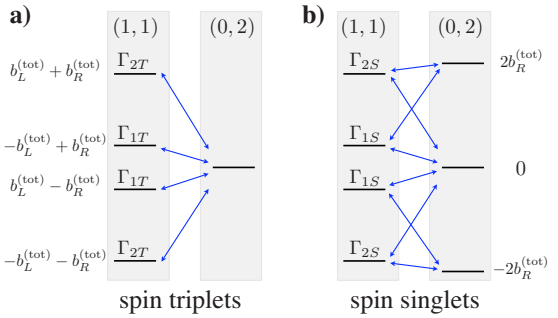

FIG. 6. (Color online) Two-electron states (lines) and their energies in a CNT DQD at strong disorder. Arrows denote tunnel couplings between (1,1) and (0,2) states. Decay rates of (1,1) states are indicated, cf. Eqs. (25) and (26) in text. Here $b_R^{(\mathrm{tot})}>b_L^{(\mathrm{tot})}$. (a) States and tunnel couplings in the five-dimensional spin-triplet subspaces. The same plot refers to all three spin-triplet subspaces. (b) States and tunnel couplings in the seven-dimensional spin-singlet subspace. (cf. Table II).

with, although each (1,1) state hybridizes only with two (0,2) states (e.g., $|K_L\uparrow,K_R\downarrow\rangle-|K_L\downarrow,K_R\uparrow\rangle$ is not coupled to $|0,K_R'\uparrow,K_R'\downarrow\rangle$ by tunneling). Due to hybridization, the four (1,1) spin-singlet states acquire two different decay rates,

$$\frac{\Gamma_{1S}}{\Gamma_R}=2t^2\left[\frac{\cos^2(\theta^{(\mathrm{tot})}/2)}{(b_L^{(\mathrm{tot})}-b_R^{(\mathrm{tot})})^2}+\frac{2\sin^2(\theta^{(\mathrm{tot})}/2)}{(b_L^{(\mathrm{tot})}+b_R^{(\mathrm{tot})})^2}\right], \tag{26a}$$

$$\frac{\Gamma_{2S}}{\Gamma_R}=2t^2\left[\frac{2\cos^2(\theta^{(\mathrm{tot})}/2)}{(b_L^{(\mathrm{tot})}-b_R^{(\mathrm{tot})})^2}+\frac{\sin^2(\theta^{(\mathrm{tot})}/2)}{(b_L^{(\mathrm{tot})}+b_R^{(\mathrm{tot})})^2}\right]. \tag{26b}$$

The rate Γ_{1S} (Γ_{2S}) corresponds to the spin-singlet states in the second and third (first and fourth) lines of Table II. We emphasize that the valley dynamics of the spin-singlet subspace is remarkably different from the valley dynamics of the spin-triplet subspaces and the spin dynamics in the spin blockade of conventional semiconductor DQDs:[43,44] in the latter cases there is only a single available (0,2) state to hybridize with, whereas in the former case there are three of them.

From now on we are aiming at deriving an analytical formula for the current in leading order in the small parameter t/b. As the next step toward that we argue that the steady-state occupations of the (0,2) states are negligible. There are two facts needed to prove this. (i) The steady-state current can be separated to contributions from single-electron tunneling via the (1,1) states and (0,2) states: $I=\Sigma_{\alpha\in(1,1)}\rho_\alpha\Gamma_\alpha+\Sigma_{\alpha\in(0,2)}\rho_\alpha\Gamma_\alpha$. For the (1,1) states, decay rates originate from a weak hybridization of the (0,2) states, therefore in the first sum, $\Gamma_\alpha\sim(t/b)^2\Gamma_R\ll\Gamma_R$. For the (0,2) states, decay rates come from direct coupling to the right lead, hence in the second sum, $\Gamma_\alpha\sim\Gamma_R$. (ii) The (0,2) states are "difficult to load" and "easy to empty," therefore, as it can be shown rigorously, their steady-state occupations are $\sim(t/b)^4$ whereas the occupations of the (1,1) states are ~1. As a result concerning the current, this means that the contributions from the (1,1) states provide the leading-order result, and the (0,2) states can be eliminated from the classical master equation [Eq. (15)].

The steady-state CME retrieved after the elimination can be solved analytically using the ansatz

$$\rho_\alpha=\frac{\Gamma_\alpha^{-1}}{\sum_{\alpha'\in(1,1)}\Gamma_{\alpha'}^{-1}},\quad[\alpha\in(1,1)], \tag{27}$$

which expresses that the occupation probability of a state is proportional to the lifetime of that state. The fact that this simple ansatz solves our classical master equation is a consequence of the equivalence of the 16 (1,1) states in the following sense: if one of those is filled randomly with a uniform distribution, then after one transport cycle the occupations are still uniformly distributed. Mathematically, the 16×16 "return probability matrix" of the (1,1) states

$$R_{\alpha\beta}=\sum_{j\in(0,1)}\frac{r_{\alpha j}}{\sum_{\alpha'}r_{\alpha' j}}\frac{p_{j\beta}}{\sum_{j'}p_{j'\beta}},\quad[\alpha,\beta\in(1,1)] \tag{28}$$

is doubly stochastic. The key observation in proving this is that the row sums of the $(1,1)\to(0,1)$ transition probability matrix $p_{j\beta}/\Sigma_{j'}p_{j'\beta}$ are equal, which is a consequence of the vanishing detuning between (1,1) and (0,2) states. Note that the connection between R and the coefficient matrix M of the CME is

$$R_{\alpha\beta}=\left(\delta_{\alpha\beta}+\frac{M_{\alpha\beta}}{\sum_{k\in(0,1)}p_{k\beta}}\right)\Bigg|_{\alpha,\beta\in(1,1)}. \tag{29}$$

Using the solution in Eq. (27) and the rates listed in Eqs. (25) and (26), we obtain an analytical formula from Eq. (16) for the steady-state current through the DQD,

$$I=e\frac{16}{6(\Gamma_{1T}^{-1}+\Gamma_{2T}^{-1})+2(\Gamma_{1S}^{-1}+\Gamma_{2S}^{-1})}. \tag{30}$$

This analytical result is compared to numerical results in Fig. 5 and a good correspondence is found. Our analytical result gives an insight on how the angle $\theta^{(\mathrm{tot})}$ influences the current: at angles close to 0 and π, i.e., at parallel and antiparallel valley-Zeeman fields on the two dots, the current is suppressed, since then either Γ_{1T} or Γ_{2T} is small and that makes the denominator in Eq. (30) large. This qualitatively explains the zero-field dip in Fig. 5 in the case of $\theta=15\pi/16$: as the magnetic field and hence Δ_v is increased, the angle $\theta^{(\mathrm{tot})}$ crosses over from $15\pi/16$ toward 0 (since the magnetic field is enforcing alignment of $\boldsymbol{b}_L^{(\mathrm{tot})}$ and $\boldsymbol{b}_R^{(\mathrm{tot})}$), starting from and ending at suppressed current values, but sweeping through a region of enhanced current.

Our conclusion of this section is that in the considered regime the magnetotransport curve shows either a zero-field dip or peak, depending on the disorder configuration. Although our analysis in this section was based on the complete absence of spin-orbit coupling and detuning between (1,1) and (0,2) states, and a perfect alignment of the magnetic field and the CNT axis, we expect no qualitative changes in the results in the case of weak spin-orbit interaction and detuning $\Delta_{\mathrm{SO}},\Delta\ll b$ and/or a small misalignment of the field, since those factors have no effect on the tunneling

amplitude and can only slightly modify our unperturbed basis states and the corresponding energies.

As discussed in Sec. IV, in recent experiments[21,22] with CNT DQDs a zero-field dip has been found with a dip width controllable by the tunneling amplitude. In the analytical and numerical results of this section, the width of the dip (predicted for certain disorder configurations) is insensitive to the tunneling amplitude because t appears in the current as a t^2 prefactor only. Therefore, we conclude that the parameter regime of the measurement was probably different from the one considered in this section. This opinion is supported by the facts that in Ref. 21 the ratio $\Delta_{\mathrm{SO}}/b \approx 7$ has been estimated and that in Sec. IV, in a different parameter regime we have found a qualitative agreement with experiments.

VI. CONCLUSIONS

We have found that in the regime of strong spin-orbit interaction, the magnetic-field dependence of the leakage current shows a zero-field dip with a width tunable by the interdot tunneling amplitude t (Sec. IV). We have shown that the ratio of the finite-field and the zero-field current is typically $I_{\max}/I_0 \lesssim 1.5$. Both the trend in the magnetotransport data (i.e., the zero-field dip) and the numerical value 1.5 agree well with those found in Ref. 21 [see Fig. 3(a) therein]. In the measurement of Ref. 22 [Fig. 3(e) therein] the qualitative behavior is similar to our prediction, but a much larger ratio, $I_{\max}/I_0 \sim 50$ has been found, which deviates significantly from the prediction of our model. This deviation might arise from the parameters of the measured sample not fitting into the parameter regime considered in Section IV (In Ref. 22, the values of spin-orbit interaction energy and valley-mixing energy have not been estimated. Interdot tunneling has been quoted as $t \sim 50$ μeV.) Another potential reason for the deviation might be that certain features and mechanisms possibly important in the spin-valley blockade are excluded from our model. A relevant mechanism might be the spin- and/or valley-relaxation due to electron-phonon interaction or electron exchange with the leads.[5,11,13,46,60] If those relaxation rates are comparable to or larger than the lead-dot tunneling rates then they could affect the transport properties. Another possibly influential effect disregarded in our model might be the emergence of strongly correlated Wigner-molecule-like states due to the strong electron-electron interaction in nanotubes,[7–9] which would imply the rearrangement of the energy level structure shown in Table I and Fig. 4 and therefore could lead to a qualitatively different transport behavior.

We have studied the influence of disorder on the spin-valley blockade in the case of small spin-orbit interaction, where the dominant energy scale is that of the short-range disorder (Sec. V). In this regime, the leakage current can show a zero-field dip or peak, depending on the disorder configuration. Although we are not aware of any measurements carried out in this regime, we think that our results might be relevant for future experiments on graphene- and silicon-based double quantum dots.

Our QD model incorporating the valley-mixing effect due to disorder can serve as a starting point for future theoretical work on CNT QDs. The fact that the valley-mixing effective Zeeman field depends on the electronic wave function and the disorder configuration felt by the electron implies that this valley-Zeeman field changes as the electron is replaced. This feature might allow for resonant electronic valley manipulation similar to recent spin manipulation experiments in conventional semiconductor QDs using spin-orbit coupling[35] and hyperfine interaction.[36] Note that in clean nanotubes, such resonant techniques do not require a magnetic field since the two valley states having the same spin are split by the spin-orbit splitting even at zero field. A further possible application of our model could be to describe the pulsed-gate experiments of Churchill *et al.*[21] which intended to infer relaxation and decoherence times of two-electron spin-valley states in a nanotube double dot. As those results have been obtained using isotope-enriched samples, incorporating the spin- and valley-mixing hyperfine interaction[10] might also be necessary.

In conclusion, we have found that spin-independent short-range disorder in carbon nanotube double quantum dots can lift the spin-valley blockade. In our transport model, we account for valley degeneracy, spin-orbit energy splitting, and disorder-induced valley mixing, which are characteristic features of nanotube quantum dots distinguishing them from their counterparts in conventional semiconductors. The main result of this work is that in the regime of strong spin-orbit interaction our model predicts a zero-field dip in the magnetic-field dependence of the leakage current, with a dip width tunable by the height of the interdot tunneling barrier. This behavior is in accordance with recent experiments. Our analysis for the regime of strong disorder, which has possible relevance for graphene- and silicon-based double quantum dots, predicts that the magnetotransport shows either a zero-field dip or peak depending on the disorder configuration.

Note added in proof. After completion and submission of this work we became aware of two related theoretical studies,[61,62] which focus on spectral properties of perfectly clean (disorder-free) CNT DQDs. The work of von Stecher *et al.*[61] also describes the effect of strong correlations on transport in the Pauli blockade regime. The purpose of the present work is to account for disorder-induced effects in the spin-valley blockade, which makes it distinct from Refs. 61 and 62.

ACKNOWLEDGMENTS

We thank DFG for financial support within Grants No. SFB 767, No. SPP 1285, and No. FOR 912.

APPENDIX A: STRONG SPIN-ORBIT COUPLING AND $\frac{b_-^2}{\Delta_{\mathrm{SO}}} \gg t$

We have shown in Sec. IV that in the regime of strong spin-orbit interaction and $\frac{b_-^2}{\Delta_{\mathrm{SO}}} \sim t$, the magnetotransport curve develops a zero-field dip with a width which is controllable by the tunneling amplitude t. Here we argue that the above condition can be relaxed and the same statement is true in the regime $\frac{b_-^2}{\Delta_{\mathrm{SO}}} \gg t$ (provided $\Delta_{\mathrm{SO}} \gg b, t, \Delta_v$).

We recall that in Sec, IV we have found that at zero field six out of the 22 two-electron states are blocked, and two out of those six show a blocked-unblocked crossover as the magnetic field is switched on. We have determined the field-dependent decay rates of these six states without using the assumption $\frac{b_-^2}{\Delta_{SO}} \sim t$, therefore those results hold in the current case $\frac{b_-^2}{\Delta_{SO}} \gg t$ as well.

The effective Hamiltonians in Eqs. (18) and (19) are also valid in the current case. However, from this point there is an important deviation in the procedure compared to Sec. IV. In the zero-energy spin-polarized subspaces [described by $H_{0,\pm}$ in Eq. (18)], the three basis state does not mix evenly but instead the (1,1) supertriplet and supersinglet states hybridize strongly with each other and these hybridized states themselves hybridize only weakly with the (0,2) supersinglet via tunneling. This leads to decay rates $\sim \frac{\Delta_{SO}^2 t^2}{b_-^4} \Gamma_R \ll \Gamma_R$ (in contrast to Sec. IV where these rates were found to be $\sim \Gamma_R$). An important point is that if $b_a \sim b_-$, which is typically true due to the random nature of the disorder-induced valley fields $\boldsymbol{b}_L$ and $\boldsymbol{b}_R$, then the decay rate $\sim \frac{\Delta_{SO}^2 t^2}{b_-^4} \Gamma_R$ is still orders-of-magnitude larger than the decay rate Γ_s of the blocked states, and therefore these states can still be considered as unblocked. The same argument applies for the six states in the zero-energy mixed-spin subspace, therefore each of those can be classified as unblocked.

From these results we conclude that in the case $\frac{b_-^2}{\Delta_{SO}} \gg t$ the set of blocked states (which determine the character of the magnetotransport curve) and the form of their decay rates are the same as found in the regime $\frac{b_-^2}{\Delta_{SO}} \sim t$, and hence the conclusions drawn there hold here as well. This finding is confirmed by numerical calculations (not shown).

APPENDIX B: STRONG SPIN-ORBIT COUPLING AND $\frac{b_-^2}{\Delta_{SO}} \ll t$

Here we argue that the zero-field magnetotransport dip, discussed in Sec. IV and Appendix A, gets smeared out if the tunneling amplitude is increased to the regime $\frac{b_-^2}{\Delta_{SO}} \ll t$ such that $t \gg b_- \sqrt{\Delta_{SO}/b_a}$. (The latter condition is stronger than the former one provided that $\boldsymbol{b}_L \neq \boldsymbol{b}_R$ and therefore $b_a \neq 0$.) As before, we restrict the discussion to the strong spin-orbit coupling regime: $\Delta_{SO} \gg b, t, \Delta_v$.

As pointed out in the analysis after Eq. (19), the blocked-unblocked crossover of the high- and low energy mixed-spin supertriplets, which gives rise to a zero-field dip in the magnetotransport, occurs around the magnetic field where $\Delta_v = \frac{t^2 b_a}{\sqrt{2} b_-^2}$. This implies that if $t \gg b_- \sqrt{\Delta_{SO}/b_a}$, then the crossover would take place only in the high-field regime $\Delta_v \gg \Delta_{SO}$ and not in the low-field regime $\Delta_v \ll \Delta_{SO}$ under consideration. As a consequence, the character of the low-field magnetotransport curve will be determined by the field-induced evolution of the slow decay rates, resulting in a parabolic peak around zero field. This finding is confirmed by numerical calculations (not shown).

[1] R. Hanson, L. P. Kouwenhoven, J. R. Petta, S. Tarucha, and L. M. K. Vandersypen, Rev. Mod. Phys. **79**, 1217 (2007).
[2] D. Loss and D. P. DiVincenzo, Phys. Rev. A **57**, 120 (1998).
[3] B. Trauzettel, D. V. Bulaev, D. Loss, and G. Burkard, Nat. Phys. **3**, 192 (2007).
[4] P. Recher, J. Nilsson, G. Burkard, and B. Trauzettel, Phys. Rev. B **79**, 085407 (2009).
[5] D. V. Bulaev, B. Trauzettel, and D. Loss, Phys. Rev. B **77**, 235301 (2008).
[6] J. Fischer, B. Trauzettel, and D. Loss, Phys. Rev. B **80**, 155401 (2009).
[7] M. Roy and P. A. Maksym, EPL **86**, 37001 (2009).
[8] A. Secchi and M. Rontani, Phys. Rev. B **80**, 041404(R) (2009).
[9] B. Wunsch, Phys. Rev. B **79**, 235408 (2009).
[10] A. Pályi and G. Burkard, Phys. Rev. B **80**, 201404(R) (2009).
[11] P. R. Struck and G. Burkard, Phys. Rev. B **82**, 125401 (2010).
[12] P. Recher and B. Trauzettel, Nanotechnology **21**, 302001 (2010).
[13] M. S. Rudner and E. I. Rashba, Phys. Rev. B **81**, 125426 (2010).
[14] S. Schnez, K. Ensslin, M. Sigrist, and T. Ihn, Phys. Rev. B **78**, 195427 (2008).
[15] J. Kong, C. Zhou, E. Yenilmez, and H. Dai, Appl. Phys. Lett. **77**, 3977 (2000).
[16] S. J. Tans, M. H. Devoret, H. Dai, A. Thess, R. E. Smalley, L. J. Geerlings, and C. Dekker, Nature (London) **386**, 474 (1997).
[17] N. Mason, M. J. Biercuk, and C. M. Marcus, Science **303**, 655 (2004).
[18] M. R. Gräber, W. A. Coish, C. Hoffmann, M. Weiss, J. Furer, S. Oberholzer, D. Loss, and C. Schönenberger, Phys. Rev. B **74**, 075427 (2006).
[19] F. Kuemmeth, S. Ilani, D. C. Ralph, and P. L. McEuen, Nature (London) **452**, 448 (2008).
[20] M. R. Buitelaar *et al.*, Phys. Rev. B **77**, 245439 (2008).
[21] H. O. H. Churchill, F. Kuemmeth, J. W. Harlow, A. J. Bestwick, E. I. Rashba, K. Flensberg, C. H. Stwertka, T. Taychatanapat, S. K. Watson, and C. M. Marcus, Phys. Rev. Lett. **102**, 166802 (2009).
[22] H. O. H. Churchill, A. J. Bestwick, J. W. Harlow, F. Kuemmeth, D. Marcos, C. H. Stwertka, S. K. Watson, and C. M. Marcus, Nat. Phys. **5**, 321 (2009).
[23] G. A. Steele, G. Gotz, and L. P. Kouwenhoven, Nat. Nanotechnol. **4**, 363 (2009).
[24] L. A. Ponomarenko, F. Schedin, M. I. Katsnelson, R. Yang, E. W. Hill, K. S. Novoselov, and A. K. Geim, Science **320**, 356 (2008).
[25] C. Stampfer, J. Güttinger, F. Molitor, D. Graf, T. Ihn, and K. Ensslin, Appl. Phys. Lett. **92**, 012102 (2008).
[26] F. Molitor, S. Dröscher, J. Güttinger, A. Jacobsen, C. Stampfer, T. Ihn, and K. Ensslin, Appl. Phys. Lett. **94**, 222107 (2009).
[27] X. Liu, J. B. Oostinga, A. F. Morpurgo, and L. M. K. Vandersypen, Phys. Rev. B **80**, 121407(R) (2009).
[28] F. Kuemmeth, H. O. H. Churchill, P. K. Herring, and C. M. Marcus, Mater. Today **13**, 18 (2010).

[29] S. J. Chorley, G. Giavaras, J. Wabnig, G. A. C. Jones, C. G. Smith, G. A. D. Briggs, and M. R. Buitelaar, arXiv:1004.4377 (unpublished).
[30] A. Rycerz, J. Tworzydlo, and C. W. J. Beenakker, Nat. Phys. **3**, 172 (2007).
[31] P. Recher, B. Trauzettel, A. Rycerz, Y. M. Blanter, C. W. J. Beenakker, and A. F. Morpurgo, Phys. Rev. B **76**, 235404 (2007).
[32] K. Flensberg and C. M. Marcus, Phys. Rev. B **81**, 195418 (2010).
[33] K. Ono, D. G. Austing, Y. Tokura, and S. Tarucha, Science **297**, 1313 (2002).
[34] F. H. L. Koppens, C. Buizert, K. J. Tielrooij, I. T. Vink, K. C. Nowack, T. Meunier, L. P. Kouwenhoven, and L. M. K. Vandersypen, Nature (London) **442**, 766 (2006).
[35] K. C. Nowack, F. H. L. Koppens, Y. V. Nazarov, and L. M. K. Vandersypen, Science **318**, 1430 (2007).
[36] E. A. Laird, C. Barthel, E. I. Rashba, C. M. Marcus, M. P. Hanson, and A. C. Gossard, Phys. Rev. Lett. **99**, 246601 (2007).
[37] J. R. Petta, A. C. Johnson, J. M. Taylor, E. A. Laird, A. Yacoby, M. D. Lukin, C. M. Marcus, M. P. Hanson, and A. C. Gossard, Science **309**, 2180 (2005).
[38] J. R. Petta, H. Lu, and A. C. Gossard, Science **327**, 669 (2010).
[39] H. Ribeiro, J. R. Petta, and G. Burkard, Phys. Rev. B **82**, 115445 (2010).
[40] D. J. Reilly, J. M. Taylor, J. R. Petta, C. M. Marcus, M. P. Hanson, and A. C. Gossard, Science **321**, 817 (2008).
[41] S. Foletti, H. Bluhm, D. Mahalu, V. Umansky, and A. Yacoby, Nat. Phys. **5**, 903 (2009).
[42] H. Ribeiro and G. Burkard, Phys. Rev. Lett. **102**, 216802 (2009).
[43] F. H. L. Koppens, J. A. Folk, J. M. Elzerman, R. Hanson, L. H. W. van Beveren, T. Vink, H. P. Tranitz, W. Wegscheider, L. P. Kouwenhoven, and L. M. K. Vandersypen, Science **309**, 1346 (2005).
[44] O. N. Jouravlev and Y. V. Nazarov, Phys. Rev. Lett. **96**, 176804 (2006).
[45] S. Nadj-Perge, S. M. Frolov, J. W. W. van Tilburg, J. Danon, Y. V. Nazarov, R. Algra, E. P. A. M. Bakkers, and L. P. Kouwenhoven, Phys. Rev. B **81**, 201305(R) (2010).
[46] J. Danon and Y. V. Nazarov, Phys. Rev. B **80**, 041301(R) (2009).
[47] O. V. Yazyev, Nano Lett. **8**, 1011 (2008).
[48] A. Pfund, I. Shorubalko, K. Ensslin, and R. Leturcq, Phys. Rev. Lett. **99**, 036801 (2007).
[49] T. Ando and T. Nakanishi, J. Phys. Soc. Jpn. **67**, 1704 (1998).
[50] A. H. Castro Neto and F. Guinea, Phys. Rev. Lett. **103**, 026804 (2009).
[51] T. Ando, J. Phys. Soc. Jpn. **69**, 1757 (2000).
[52] N. Shaji *et al.*, Nat. Phys. **4**, 540 (2008).
[53] D. Culcer, L. Cywiński, Q. Li, X. Hu, and S. Das Sarma, Phys. Rev. B **80**, 205302 (2009).
[54] D. Culcer, L. Cywinski, Q. Li, X. Hu, and S. Das Sarma, arXiv:1001.5040 (unpublished).
[55] M. Friesen and S. N. Coppersmith, Phys. Rev. B **81**, 115324 (2010).
[56] H.-P. Breuer and F. Petruccione, *The Theory of Open Quantum Systems* (Oxford University Press, New York, 2002).
[57] P.-O. Löwdin, J. Chem. Phys. **19**, 1396 (1951).
[58] F. Qassemi, W. A. Coish, and F. K. Wilhelm, Phys. Rev. Lett. **102**, 176806 (2009).
[59] In the original work of Löwdin (Ref. 57), the effective Hamiltonians derived for degenerate subspaces depend on the energy itself, leading to equations to be solved self-consistently. In this work, we always approximate the energy in the effective Hamiltonian as the unperturbed energy of the considered subspace, which results in an energy-independent effective Hamiltonian.
[60] A. B. Vorontsov and M. G. Vavilov, Phys. Rev. Lett. **101**, 226805 (2008).
[61] J. von Stecher, B. Wunsch, M. Lukin, E. Demler, and A. M. Rey, Phys. Rev. B **82**, 125437 (2010).
[62] S. Weiss, E. I. Rashba, F. Kuermeth, H. O. H. Churchill, and K. Flensberg, e-print arXiv:1006.0724, Phys. Rev. B (to be published).